Highlights

Nonlinear Topology Optimization on Thin Shells Using a Reduced-Order Elastic Shell Model

Fan Feng,Shiying Xiong,Hiroki Kobayashi,Yuqing Zhou,Masato Tanaka,Atsushi Kawamoto,Tsuyoshi Nomura,Bo Zhu

- Topology optimization on geometrically nonlinear thin shells.

- Adopting discrete shell based on discrete differential geometry for a reduced degree of freedom.

- High-resolution topologically complex thin shell structures on free-form surfaces subject to bending and stretching loads with large nonlinear deformations

Nonlinear Topology Optimization on Thin Shells Using a Reduced-Order Elastic Shell Model

Fan Feng[a,*], Shiying Xiong[e,a], Hiroki Kobayashi[b], Yuqing Zhou[c], Masato Tanaka[b,c], Atsushi Kawamoto[b], Tsuyoshi Nomura[b] and Bo Zhu[d,a]

[a]*Computer Science Department, Dartmouth College, Hanover, New Hampshire, 03755, United States*

[b]*Toyota Central R&D Labs., Inc., Nagakute, Aichi, 480-1192, Japan*

[c]*Toyota Research Institute of North America, Ann Arbor, Michigan, 48105, United States*

[d]*School of Interactive Computing,College of Computing,Georgia Institute of Technology, Atlanta, GA, 30332, United States*

[e]*Department of Engineering Mechanics, School of Aeronautics and Astronautics, Zhejiang University, Hangzhou, Zhejiang, 310027, China*

ARTICLE INFO

Keywords:
Topology optimization
Shell reinforcement
Geometric nonlinearity
Discrete geometric shell

ABSTRACT

We present a novel numerical algorithm to perform nonlinear topology optimization on elastic thin shells. The main component of our method is a differentiable thin-shell simulator based on discrete differential geometry (DDG) discretization and the projected Newton method to solve geometrically nonlinear elasticity and its derivatives on a triangle mesh. We build a density-based topology optimization algorithm, enhanced by a density filter and a Heaviside projection scheme, to emerge and optimize topologically complex shell structures on curved surfaces. We validate our approach using standard test cases for nonlinear topology optimization and demonstrate the efficacy of our method by tackling highly nonlinear topology optimization problems by producing complex and high-resolution shell structural designs under various load conditions.

1. Introduction

Thin-shell structures manifest outstanding stiffness-to-weight ratios compared with their volumetric counterparts and therefore have played an essential role in many weight-sensitive design applications such as automobiles and airplanes. The design of thin shell structures has received increasing attention in both computational design and topology optimization communities over the past decades, exemplified by the differentiable simulation and inverse design of various kinds of functional shells, such as fuselage and Lotte tower [1], ankle-foot orthosis [2], blunt cone shell [3] and etc. However, the state-of-the-art works that optimize thin-shell topology with fine features concentrate on shell topology optimization with linear elasticity. Devising methods to tackle both topological complexities and geometric nonlinearities in a unified framework remains challenging.

Researchers in mechanical engineering and scientific computing developed a host of algorithms and commercial software (e.g. Comsol [4]) to solve thin-shell mechanics. Originated from the Mixed Interpolation of Tensorial Components (MITC) [5] approach, one of the well-received models using triangular elements that facilitate shell analysis and design is MITC3 [6] and its nonlinear extension MITC3+ [7]. The linear [8] and non-linear [9] geometric effects of MITC3 have been well-studied.

On the other side, thin-shell simulation has also drawn extensive attention from computational physics and computational geometry researchers for decades, since the seminal work [10] on discretizing and simulating elastic surfaces. A line of pioneering research has been done to devise effective variational solvers and robust time integrators to simulate shell dynamics on a triangle mesh [11, 12, 13, 14]. Along this line, researchers started to explore solvers based on Discrete Differential Geometry (DDG) [15] and intrinsic shell models [16], where DDG developed discrete versions of fundamental concepts from differential geometry, such as curvature, tangents, and gradients, that can be applied to discrete geometric structures like meshes, graphs, and point clouds. Our shell simulator follows this line of research by discretizing the membrane and bending energy terms on a triangle mesh and solving its equilibrium by minimizing the energy.

Volumetric topology optimization has received tremendous success over the past decades [17, 18, 19]. Combined with additional geometric constraints, volumetric approaches have been used to design manifold-coated structures with enclosed shells [20, 21, 22, 23], thin sheet metal structures tailored for the deep drawing manufacturing process [24], generalized 3D non-manifold thin-walled structures [25], and sparse lattice structures [26, 27]. They have also been employed to produce thin features [28] or cellular structures [29] on a planar domain. However, none of these works leverage the shell model's geometric feature to reduce computational cost.

Compared with the volumetric topology optimization counterpart, topology optimization on shells or other codimensional geometries has remained less explored. Early work [30] started by optimizing thickness as a varying field.

*Corresponding author

✉ fan.feng.gr@dartmouth.edu (F. Feng); shiying.xiong@zju.edu.cn (S. Xiong); hiroki.kobayashi@mosk.tytlabs.co.jp (H. Kobayashi); yuqing.zhou@toyota.com (Y. Zhou); tanamasa@mosk.tytlabs.co.jp (M. Tanaka); atskwmt@mosk.tytlabs.co.jp (A. Kawamoto); nomu2@mosk.tytlabs.co.jp (T. Nomura); bo.zhu@dartmouth.edu (B. Zhu)

ORCID(s):

Ansola et al. [31] introduced a parametric method to co-optimize the shell shape and topology with microstructure. A discrete material optimization framework [32] later was proposed to optimize material on laminated shells, followed by extensions [33][34]. There is some more recent progress made using different topology representations. Ho and Kim[35] co-optimized the shape and topology of a linear thin shell using the level-set method. Other examples include NURBS [36] and Moving Morphable Components (MMC) [3], series expansion [37], and multi-layer representations [38] to obtain shell topology optimization results. We want also to highlight the work done by [1], which optimized shells with millions of elements on a supercomputer. Their approach produced the state-of-the-art resolution for thin-shell optimization, although with their focus on optimizing linear shells.

Despite the progress in optimizing shell structures using different topological representations, producing high-quality topology optimization designs on a geometrically nonlinear thin shell remains challenging, due to multiple interleaving difficulties in practice to simultaneously tackle the shell's geometric nonlinearity and topological complexities to probe novel shell structural designs. In particular, due to the coupling between the shell's bending and stretching mechanics, obtaining clear, binary structures is not a trivial task. The local minima in a nonlinear shell could exhibit features with creases, articulated joints, or a mix of surfaces and beams, which are drastically different in terms of both optimization convergence and mechanical performance from their linear and volumetric counterparts.

Several methods have been investigated to solve the convergence problem with non-linear topology optimization including using the relaxed convergence criterion [39], interpolation with linear energy [40], linear to nonlinear two-step process [41], element removal and reintroduction [42, 43], and the co-rotational scheme [44]. However, these methods either add on excess computational costs or require significant implementation efforts. Similarly, our method solves the convergence issue of the thin-shell simulation within the SIMP framework by the projected Newton's method but with minimal modification of the nonlinear structural optimization framework to keep their simulation performance.

On the other hand, a multitude of recent work in computational design and fabrication communities has been devoted to the inverse design of functional thin shells. These works can be categorized according to their physical design variables and optimization focus, including the shape-material co-optimization [45], magnetoelasticity co-optimization [46], parametric shapes [47], shell reinforcement [48, 49], and synthesized microstructures [50, 51, 52], to name just a few. While they are proposed to solve different problems of inverse design, none of them has studied the topology optimization on thin shells.

We present a novel topology optimization algorithm to facilitate nonlinear structural design on thin shells. We build our approach upon state-of-the-art nonlinear DDG shell simulators stemming from previous work in computational physics and geometry [15, 16] and extend the framework to support differentiation calculation by adopting the projected Newton method. We further incorporate this differentiable solver into a topology optimization pipeline by equipping density representations, binary filters, and large-scale optimizers in a unified framework. Our method provides a practical tool that enables the topological design of complex and nonlinear thin-shell structures, which, to the best of our knowledge, produces state-of-the-art nonlinear shell topology optimization results in terms of their design complexity.

The rest of the paper is organized as follows. In Section 2, we introduce the thin-shell model that we adopt and the quasi-static simulation algorithm using the projected Newton method. We then formulate the topology optimization problem, derive the sensitivities with the given thin-shell model and present the optimization algorithm in Section 3. In Section 4, we validate our method by several simple cases and then demonstrate the efficacy of our method with more complicated boundary conditions, before conclusions are drawn in Section 5.

2. Thin-shell Model

2.1. Continuous Model

Based on the Kirchhoff–Love assumption, we model a thin shell with a mid-surface $\boldsymbol{f} : \Omega \rightarrow \mathbb{R}^3$ extended by a constant thickness h. Here $\boldsymbol{f}$ is a mapping from the two-dimensional parameter space Ω to a three-dimensional space $\mathbb{R}^3$. We represent the shell volume in terms of the shell's mid-surface $\boldsymbol{f}$ as $\boldsymbol{x}(x, y, z) = \boldsymbol{f}(x, y) + z\boldsymbol{n}(x, y)$, where $\boldsymbol{n}$ is the mid-surface normal, x and y are local coordinates in Ω, $\boldsymbol{x}$ is the coordinate in $\mathbb{R}^3$, and $z \in [-h/2, h/2]$ is the normal extension. The first and the second fundamental forms on $\boldsymbol{f}$ are then calculated as

$$\mathrm{I} = \begin{bmatrix} \frac{\partial \boldsymbol{f}}{\partial x} \cdot \frac{\partial \boldsymbol{f}}{\partial x} & \frac{\partial \boldsymbol{f}}{\partial x} \cdot \frac{\partial \boldsymbol{f}}{\partial y} \\ \frac{\partial \boldsymbol{f}}{\partial x} \cdot \frac{\partial \boldsymbol{f}}{\partial y} & \frac{\partial \boldsymbol{f}}{\partial y} \cdot \frac{\partial \boldsymbol{f}}{\partial y} \end{bmatrix}, \ \mathrm{II} = -\begin{bmatrix} \frac{\partial \boldsymbol{n}}{\partial x} \cdot \frac{\partial \boldsymbol{f}}{\partial x} & \frac{\partial \boldsymbol{n}}{\partial x} \cdot \frac{\partial \boldsymbol{f}}{\partial y} \\ \frac{\partial \boldsymbol{n}}{\partial x} \cdot \frac{\partial \boldsymbol{f}}{\partial y} & \frac{\partial \boldsymbol{n}}{\partial y} \cdot \frac{\partial \boldsymbol{f}}{\partial y} \end{bmatrix} . \quad (1)$$

Following [15, 16], we adopt the St. Venant-Kirchhoff model and define the elastic energy density using the first and second fundamental forms:

$$e = \frac{h}{4} \left\| \bar{\mathrm{I}}^{-1}(\mathrm{I} - \bar{\mathrm{I}}) \right\|_M \sqrt{\det \bar{\mathrm{I}}} + \frac{h^3}{12} \left\| \bar{\mathrm{I}}^{-1}(\mathrm{II} - \bar{\mathrm{II}}) \right\|_M \sqrt{\det \bar{\mathrm{I}}}. \quad (2)$$

Here, the bar notation denotes variables in the rest shape. The first term in Eq. (2) accounts for the stretching energy, and the second term represents the bending energy. We choose the material norm $\|\cdot\|_M$ by following the formula used in [15] as:

$$\|A\|_M = \frac{E}{1 - \nu^2} \left[\nu \operatorname{Tr}(A)^2 + (1 - \nu) \operatorname{Tr}\left(A^2\right) \right], \quad (3)$$

where A is a 2×2 matrix, E is the Young's modulus and ν is the Poisson's ratio.

2.2. Differential Geometry Discretization

We discretize the elastic energy on a triangle mesh (V, E, F), where V, E, and F are the sets of vertices, edges, and faces, respectively. We assume that the physical quantities and the rest counterparts are constant over each face of the triangle mesh. Following [16] adopting the use of DDG, for a triangle with vertices v_i, v_j, v_k, we discretize $\mathrm{I}(x, y)$ and $\mathrm{II}(x, y)$ into
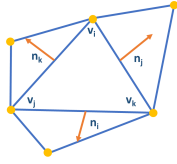
$$\mathrm{I}_{ijk} = \begin{bmatrix} \|v_j - v_i\|^2 & (v_j - v_i) \cdot (v_k - v_i) \\ (v_j - v_i) \cdot (v_k - v_i) & \|v_k - v_i\|^2 \end{bmatrix}, \quad (4)$$

and

$$\mathrm{II}_{ijk} = \frac{1}{2} \begin{bmatrix} (n_j - n_i) \cdot (v_j - v_i) & (n_j - n_i) \cdot (v_k - v_i) \\ (v_j - v_i) \cdot (n_k - n_i) & (v_k - v_i) \cdot (n_k - n_i) \end{bmatrix}, \quad (5)$$

where (n_i, n_j, n_k) are the mid-edge normal. We can also compute the rest first and second fundamental forms analogously for a given rest configuration $(\bar{v}_i, \bar{v}_j, \bar{v}_k)$ and $(\bar{n}_i, \bar{n}_j, \bar{n}_k)$. Then it is straightforward to write down a discrete elastic energy density for each triangle by substituting (4) and (5) into (2).

2.3. Quasi-static Simulation

We devise a quasi-static solver to minimize the elastic energy defined in Eq. (2) with given boundary conditions and external loads. Solving the quasi-static system using the implicit Euler scheme amounts minimizing the total potential energy $e' = e - f_{ext} \cdot x$ on a discrete shell, which is nonlinear w.r.t. the vertex positions. We devised an iterative solver based on the Newton–Raphson method with a backtracing line search to find the solution with more numerical stability. As shown in Algorithm 1, in each iteration we first compute the total potential energy and the corresponding gradients and Hessian. Since the energy, derivatives, and Hessian are calculated on each triangle separately, we can easily parallelize the computation using multi-threads on the CPU to reach high computational efficiency, using OpenMP [53]. The system's Hessian matrix needs to be positive semi-definite (PSD) to ensure the algorithm searches in an energy-descending direction. We achieve this by performing eigen-decomposition on the Hessian matrix of each triangle and clamping the negative eigenvalues to zero (similar ideas can be seen in [54]). After obtaining the symmetric PSD global hessian matrix and gradients, we solve the linear system (Line 5) using the CHOLMOD [55] library. We check for the convergence of the simulation based on the maximum displacement norm and the tolerance is set to be $1e - 4$ of the typical edge length (Line 6) unless indicated otherwise. We then perform the backtracking line search to check if the potential energy after the vertices update is smaller than the potential energy at the starting point to achieve better stability. If the potential energy doesn't decrease, we half the step size and continue the process.

Algorithm 1 Quasi-static Thin Shell Simulation
1: **for** $i \leftarrow 1$ to max_iterations **do**
2:      $e' \leftarrow compute\_potential(\boldsymbol{x})$
3:      $\boldsymbol{H} = project\_PSD(\frac{\partial^2 e}{\partial \boldsymbol{x}^2})$
4:      $\boldsymbol{b} = \boldsymbol{f}_{ext} - \frac{\partial e}{\partial \boldsymbol{x}}$
5:      $\Delta \boldsymbol{x} = LinearSolve(\boldsymbol{H}, \boldsymbol{b})$
6:      **if** $\|\Delta \boldsymbol{x}\|_\infty < tol$ **then**
7:          **break**
8:      **end if**
9:      $e'_{tmp} \leftarrow compute\_potential(\boldsymbol{x} + \Delta \boldsymbol{x})$
10:     $\alpha = 1$
11:     **while** $e'_{tmp} \geq e'$ **do**
12:         $e'_{tmp} \leftarrow compute\_potential(\boldsymbol{x} + \alpha \Delta \boldsymbol{x})$
13:         $\alpha /= 2$
14:     **end while**
15:     $e' = e' \leftarrow tmp$
16:     $\boldsymbol{x} \leftarrow \boldsymbol{x} + \alpha \Delta \boldsymbol{x}$
17: **end for**

---

3. Topology Optimization

3.1. Problem Formulation

Design variables We define a density value $\rho \in [0, 1]$ on each triangle. Following the modified Solid Isotropic Material with Penalization (SIMP) method [17], Young's modulus of each triangle is calculated as a function of input density with a constant penalizing power p as:

$$E(\rho) = E_{\min} + \rho^p(E_0 - E_{\min}), \quad (6)$$

where $E_{\min}$ and E_0 are constants specifying the minimum and maximum Young's modulus, and ρ is a scalar field discretizing the density distribution over triangles. If filters are further applied on ρ, Eq.(6) will take the projected density as input. We choose $E_{\min} = 1e - 6E_0$, E_0 specified in the Table 1 and p varies according to description in Subsection 3.3.

Optimization problem Given a domain Ω, we formulate the topology optimization problem as minimizing the structural compliance $e(\rho, \boldsymbol{u})$ by optimizing ρ, when the force equilibrium of internal force $-\partial e / \partial \boldsymbol{u}$ and external force $\boldsymbol{f}_{ext}$ is reached:

$$\underset{\rho}{\text{minimize}} \; e(\rho, \boldsymbol{u}), \quad \text{subject to} \quad \begin{cases} \dfrac{V(\rho)}{V(\Omega)} \leq f_v, \\ \boldsymbol{D}\boldsymbol{u} = \boldsymbol{0}, \\ \dfrac{\partial e}{\partial \boldsymbol{u}} = \boldsymbol{f}_{ext}, \end{cases} \quad (7)$$

where $\boldsymbol{u}$ is the displacement, $V(\rho)$ is the material volume, $V(\Omega)$ is the volume of the design domain, f_v is the input volume fraction constraint, $\boldsymbol{D}$ is a selection matrix assigning Dirichlet boundary conditions to mesh nodes.

Density filters We devised a mesh-independent density filter and a projection filter to coerce the density field toward

forming a clear structure. The combination of these two steps also avoids checkerboard artifacts. The first pass we employed is to smooth the density field. Motivated by [56], we calculate a weighted average density based on triangles within a certain range. For a given triangle k, our filter is calculated as:

$$\tilde{\rho}_k = \frac{\sum_{i \in N_k} w_{ki} \varphi_i v_i}{\sum_{i \in N_k} w_{ki} v_i}, \tag{8}$$

$$w_{ki} = r - |\mathbf{x}_k - \mathbf{x}_i|, \tag{9}$$

which blends the densities within a spherical neighborhood specified by the radius r. Here N_k is the k-th element of the neighbor list within r, v_i is the triangle area, and φ_i is the triangle density. For the second pass, we apply a projection filter to obtain a binary result of the final density field on the triangle mesh. Our scheme was motivated by the projection approach used in volumetric topology optimizations (e.g. [57]) to obtain a clear structure. The projection filter takes $\tilde{\rho}$ as the input from the previous filter and calculates the projected density $\hat{\rho}$ as:

$$\hat{\rho}_k = \frac{\tanh(\gamma \eta) + \tanh\big(\gamma(\tilde{\rho}_k - \eta)\big)}{\tanh(\gamma \eta) + \tanh(\gamma(1 - \eta))}, \tag{10}$$

where $\eta = 0.5$ is the density threshold and γ controls how strong the projection is. When $\gamma = 1$, there is no projection. In our implementation, we use $\gamma \in [1, 16]$. Last, we set the projected density value $\hat{\rho}$ as the input of Eq. (6) to update Young's modulus of each triangle.

Algorithm 2 Thin Shell Topology Optimization

1: $p \leftarrow 1, \gamma \leftarrow 1, \rho_e \leftarrow f_v \forall e \in \Omega$
2: **for** $i \leftarrow 1$ to max_iterations **do**
3:     Increment p and γ with the continuation scheme
4:     Update $\mathbf{x}$ according to Algorithm 1
5:     Calculate e using Equation 2
6:     Calculate $V(\rho)$
7:     Update $\frac{\partial e}{\partial \tilde{\rho}_i}$ and $\frac{\partial V(\rho)}{\partial \tilde{\rho}_i}$ using Equation (18) and (19)
8:     $\rho_{i+1} \leftarrow mma\_update(\rho_i, \partial \frac{e}{\rho_i}, V(\rho), \partial \frac{V(\rho)}{\rho_i}, move\_limit)$
9:     $\Delta \rho \leftarrow \rho_{i+1} - \rho_i$
10:     **if** $\|\Delta \rho\|_\infty < tol$ **then** $\triangleright tol = 1e{-}4$
11:         **break**
12:     **end if**
13:     Update $\hat{\rho}$ using Equation (8) and (10)
14: **end for**

3.2. Sensitivity

Since both the displacements of vertices $\mathbf{u}$ and the density field ρ influence the elastic energy, we have

$$\frac{\partial e(\mathbf{u}, \rho)}{\partial \mathbf{u}} = f_{ext}. \tag{11}$$

By taking the partial derivative of ρ and right multiplying $[\partial^2 e(\mathbf{u}, \rho)/\partial \mathbf{u}^2]^{-1}$ for the Eq. (11), we derive the partial derivative of $\mathbf{u}$ with respect to ρ as follows

$$\frac{\partial \mathbf{u}}{\partial \rho} = -\frac{\partial^2 e(\mathbf{u}, \rho)}{\partial \rho \partial \mathbf{u}} \left[\frac{\partial^2 e(\mathbf{u}, \rho)}{\partial \mathbf{u}^2}\right]^{-1}. \tag{12}$$

Substituting (12) into the total derivative of objective e w.r.t. ρ

$$\frac{\mathrm{d}e(\mathbf{u}, \rho)}{\mathrm{d}\rho} = \frac{\partial e(\mathbf{u}, \rho)}{\partial \rho} + \frac{\partial \mathbf{u}}{\partial \rho} \frac{\partial e(\mathbf{u}, \rho)}{\partial \mathbf{u}} \tag{13}$$

yields

$$\frac{\mathrm{d}e(\mathbf{u}, \rho)}{\mathrm{d}\rho} = \frac{\partial e(\mathbf{u}, \rho)}{\partial \rho} - \frac{\partial^2 e(\mathbf{u}, \rho)}{\partial \rho \partial \mathbf{u}} \left[\frac{\partial^2 e(\mathbf{u}, \rho)}{\partial \mathbf{u}^2}\right]^{-1} \frac{\partial e(\mathbf{u}, \rho)}{\partial \mathbf{u}} \tag{14}$$

Notice that we do not calculate the inverse of the matrix directly. Instead, we convert $\left[\frac{\partial^2 e(\mathbf{u}, \rho)}{\partial \mathbf{u}^2}\right]^{-1} \frac{\partial e(\mathbf{u}, \rho)}{\partial \mathbf{u}}$ into solving the linear system and solve it with the CHOLMOD solver as what we did in the forward simulation. Using (6), (14) can be simplified as

$$\frac{\partial e}{\partial \rho_k} = p \rho_k^{p-1} e_k. \tag{15}$$

From (10), we have

$$\frac{\partial \hat{\rho}_k}{\partial \tilde{\rho}_k} = \gamma \frac{1 - \tanh\big(\gamma(\tilde{\rho}_k - \eta)\big)^2}{\tanh(\gamma \eta) + \tanh(\gamma(1 - \eta))} \tag{16}$$

Here, $\partial \bar{\rho}_k / \partial \varphi_j$ is calculated using (8) as

$$\frac{\partial \rho_k}{\partial \varphi_j} = \frac{w_{ki} v_j}{\sum_{i \in N_e} w_{ki} v_i}, j \in N_e \tag{17}$$

Following the chain rule, the derivative of objective e w.r.t design variables φ is

$$\frac{\partial e}{\partial \varphi_j} = \frac{\mathrm{d}e}{\mathrm{d}\hat{\rho}_k} \frac{\partial \hat{\rho}_k}{\partial \tilde{\rho}_k} \frac{\partial \tilde{\rho}_k}{\partial \varphi_j}. \tag{18}$$

The derivative of volume $V(\rho_k)$ w.r.t. φ_j is simply the volume of each element times $\frac{\partial \hat{\rho}_k}{\partial \tilde{\rho}_k}$ and $\frac{\partial \tilde{\rho}_k}{\partial \varphi_j}$, following the chain rule as

$$\frac{\partial V(\rho)}{\partial \varphi_j} = V(\hat{\rho}_k) \frac{\partial \hat{\rho}_k}{\partial \tilde{\rho}_k} \frac{\partial \tilde{\rho}_k}{\partial \varphi_j}. \tag{19}$$

3.3. Optimization

Given the sensitivities for the objective and constraints, we use the method of moving asymptotes (MMA) [58, 59] to optimize the densities on triangles to minimize the shell's elastic compliance. Following Algorithm 2, we first initialize the penalization power p and the density projection parameter γ to 1. In each iteration, we then run the quasi-static thin-shell simulation according to Algorithm 1 to reach

a balance between internal and external forces under the current density distribution. On Line 3, to achieve better density convergence we use the continuation strategies as [60] by increasing p by 0.05 every other iteration when p is smaller than 2 and once every five iterations when p is smaller than 3. Similarly, we double γ once every 10 iterations after 200 iterations until it reaches 16. Then we calculate the sensitivities for the objective and constraint functions according to Equation (18) and (19) to update the optimization variables. Also, we do not perform a direct inversion on the global Hessian matrix but solve for $\frac{\partial u}{\partial \rho}$ with the corresponding linear system by Equation (12). The Hessian is calculated the same as what we do in the quasi-static simulation except that we do not project the Hessian to PSD here and switch to a direct sparse LU solver when the CHOLMOD solver fails to solve the system, in order to achieve more accurate gradients while keeping the solving efficiency at the same time. We update ρ with the MMA optimizer and check for convergence. The *move_limit* on Line 8 indicates how much the variable can change, which we use 0.1 in all experiments.

4. Numerical Results

All examples were run on a single desktop with an AMD Ryzen 7 3800X 8-Core 3.90 GHz processor and 64GB installed RAM. The experiment parameters and statistics are summarized in Table 1. Use the compliance convergence criteria $\frac{|e_{t+2}+e_{t+3}-e_t-e_{t+1}|}{e_t+e_{t+1}} < 1\%$ (subscript denotes iteration), all our examples converge within 125 iterations. The convergence plots for all examples also demonstrate good convergence. We show the results at iteration 250 after the designs become the most binary.

4.1. Validation

First, we validate the correctness of our method under different loading conditions with three examples and compared the results with other standard methods.

Long beam: validation for in-plane force As shown in Figure 1, we demonstrate that our method can produce optimization results under in-plane point force loads with different magnitudes to explore the material's geometric non-linearity. In a 4 m × 0.5 m domain with 0.001 m thickness, we set up a $160k$ triangle mesh based on an 800×100 grid with left and right nodes fixed. A point force pointing downward is added on the bottom middle node of the plane. The convergence plot of this example is shown accordingly in Figure 2, from which we can tell that all optimizations converge within 100 iterations. The initial rise in objective was due to the use of the continuation of the parameter scheme for *p*. As the force becomes larger, there are fewer detailed structures formed and buckling happens in the middle of the beam when $\|f_{ext}\| = 100N$. As the force becomes larger, the strain enters the geometrically non-linear region and the structure becomes more degenerated
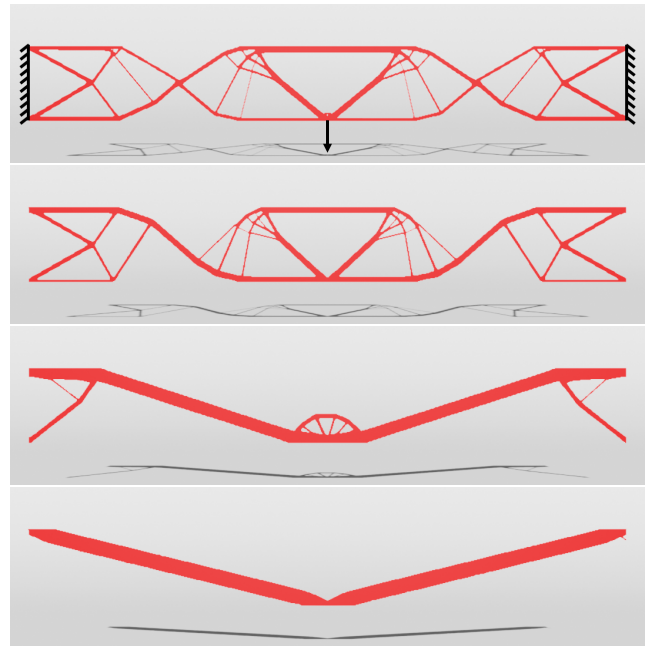

Figure 1: Optimized long beam with geometrically nonlinear elements, displacements are incorporated in the rendering. The boundary condition is illustrated using black marks on the top figure. Forces from top to bottom: 0.01N, 0.1N, 1N, and 100N. The final objectives of the structures are 4.18e-9, 4.27e-07, 4.96e-05, and 0.560 respectively.
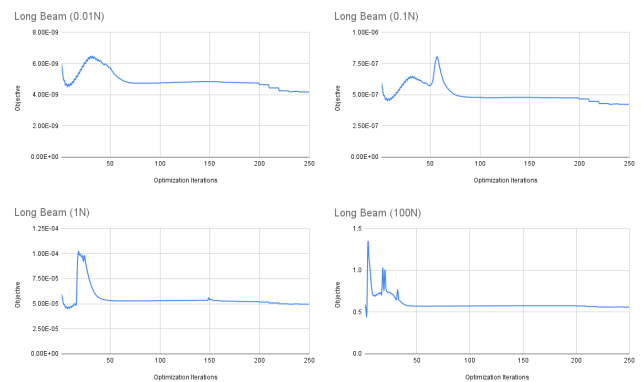

Figure 2: The convergence plots for the long beam examples.

and only supports well for the specific load case. The transition of structures from thin patterns to thick beams under different in-plane loads is consistent with the beam structures obtained by other standard nonlinear topology optimization algorithms using volumetric elements (e.g. [61]).

To further validate the correctness of our in-plane model, we further compared the results with the linear MITC3 elements in COMSOL. As shown in Figure 3, the long rectangular domain is similarly fixed on both sides and a 100 N external force load is applied on the bottom middle node. The optimized structure is similar to the structure that we optimized using a small force load equal to $0.01N$. This structure produces a much larger objective (3.59) than
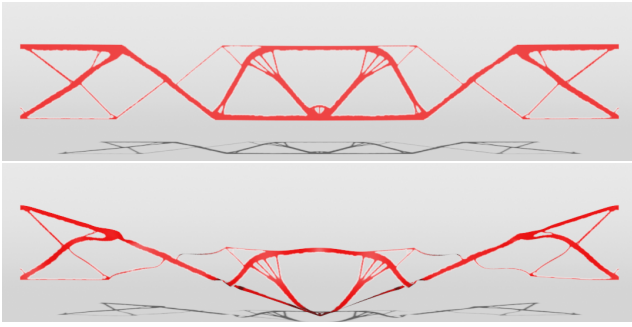
Figure 3: Top: the long beam structure produced by using linear MITC elements in COMSOL with $\|f_{ext}\| = 100N$. Bottom: the deformed structure simulated using our geometrically nonlinear simulator with an objective equal to 3.59.

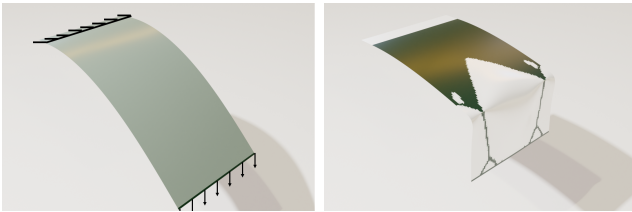that of our structure (0.560) when both are simulated with geometrically nonlinear elements.

Figure 4: Flat plane is loaded with the downward forces on the rightmost nodes. Left: highly bent plane with 100N force load. Right: the optimized structure.
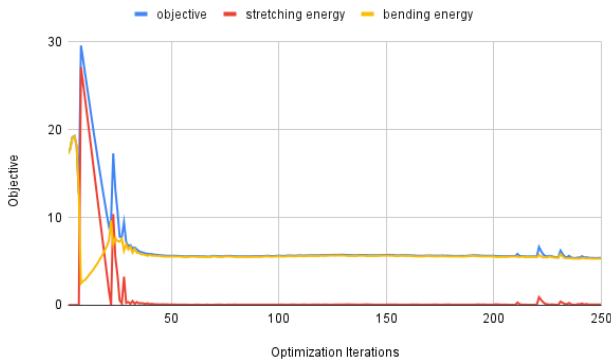

Figure 5: The convergence plot for the bending plane example.

Bending plane: validation for out-of-plane force. In this example, we demonstrate that our method can optimize structures with purely out-of-plane forces, see Figure 4. We set a triangulated 128×64 plane fix the left ten percent of the plane nodes and add 100N on the rightmost nodes with the density ρ of the rightmost faces fixed at 1. Since the displacement is very large for this example, we decrease the tolerance for simulation tolerance to 0.1 of the typical edge length for faster convergence. Before the structural

optimization, the plane with evenly distributed density is bent downwards. As optimization proceeds, densities are mostly gathered toward the left side of the structures and only minimum densities are allocated to form a connection with the force loads. Therefore, as shown in the convergence plot Figure 5, the bending energy is largely reduced and a crease traverses through the middle of the optimization domain.

Figure 6: Cylinder with top and bottom nodes fixed and pulling force (100N) distributed on two sides. Left: the initial deformation before topology optimization with boundary condition marked in black. Right: the optimized structure.
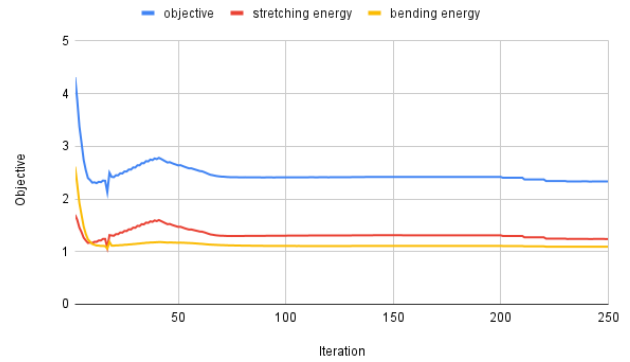

Figure 7: The convergence plot for the pulled cylinder example.

Cylinder pulled from two sides: validation for large deformation With the top and bottom nodes fixed, we add two loads of vertically distributed forces on the sides concentrating on the middle 0.5 of the cylinder height. The cylinder is $3m$ tall with a radius equal to $1m$. As demonstrated in Figure 6, there is subtle deformation can be observed initially, where the two sides are pulled by forces. At the end of the optimization, we can see two clear "X" shapes forming around the applied force while connecting the top and bottom fixed nodes. Notice that there is a vertical gap formed in each of the x shapes, which acts as a hinge so that the overall bending energy can be minimized, see plot in Figure 7.

Example	Design DoF	Sim DoF	Computation Time (ms/iter)			Newton's Iterations	$h(m)$	$E_0(Pa)$	v	f_v
			Forward	Gradient	Other					
Long beam	$160k$	$243k$	-	-	-	-	0.001	$1e^9$	0.35	0.2
Bending plane	$16k$	$25k$	3091	1188	14.377	1200	0.01	$1e^9$	0.3	0.5
Pulled cylinder	$103k$	$156k$	36411	4695	11.271	2616	0.001	$1e^9$	0.3	0.35
Paraboloid shell	$205k$	$309k$	4930	3098	68.118	2172	0.01	$1e^9$	0.5	0.5
Odonata wing 5 degree	$683k$	$1,029k$	41528	22339	509	585	0.01	$1e^9$	0.3	0.3
Odonata wing down	$683k$	$1,029k$	76961	21877	549	937	0.01	$1e^9$	0.3	0.3
Hyperboloid cylinder (concave)	$670k$	$1,006k$	38581	24465	470.164	501	0.001	$1e^5$	0.3	0.5
Hyperboloid cylinder (convex)	$670k$	$1,006k$	35310	24895	512.461	500	0.002	$1e^5$	0.3	0.5
Bunny	$139k$	$209k$	6787	4416	102.90	500	0.02	$1e^9$	0.3	0.35

Table 1
Statistics for all examples.
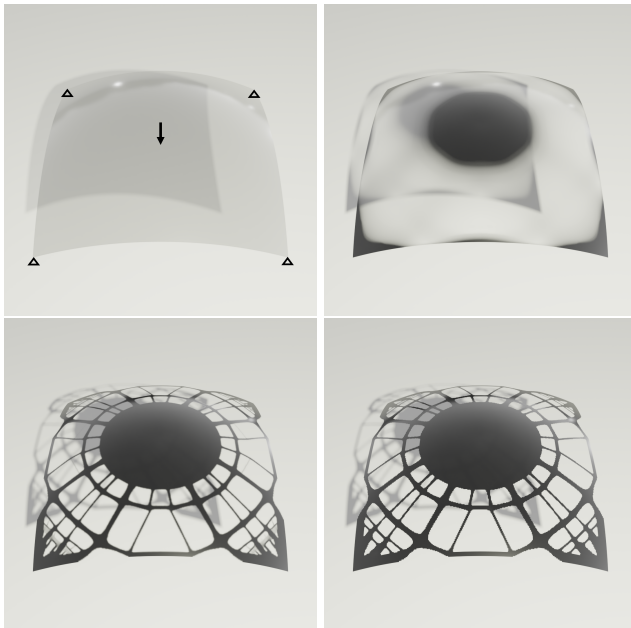
Figure 8: Paraboloid shell. Optimization iteration from left to right, top to bottom: 0, 20, 100, 250.

Figure 9: The convergence plot of the paraboloid shell example.

middle part with the four corners. The convergence plot is shown as Figure 9, from which we can observe the increase of objective before iteration 50 due to the effect of the continuation of the parameter scheme.

Figure 10: Left is the concave hyperboloid cylinder and right is the convex hyperboloid cylinder. The inset picture indicates the boundary condition.

4.2. Examples

Next, we demonstrate that our method can generate intricate structures on complex geometries under various loading conditions.

Paraboloid shell We set up a $215k$ triangle mesh with a paraboloid shape with $y = -0.5((x - 0.5)^2 + (z - 0.5)^2)$, where $x, z \in [0, 1]$. The four corners of the mesh are fixed and a downward point load of $0.0001N$ is added in the center of the mesh. As shown in Figure 8, our method first distributes the density mostly in the middle and around the four edges and then generates thin beams connecting the
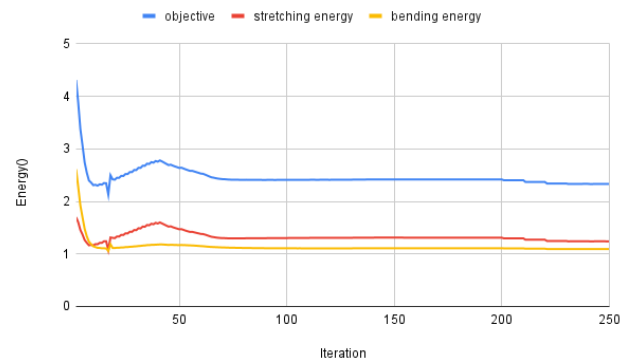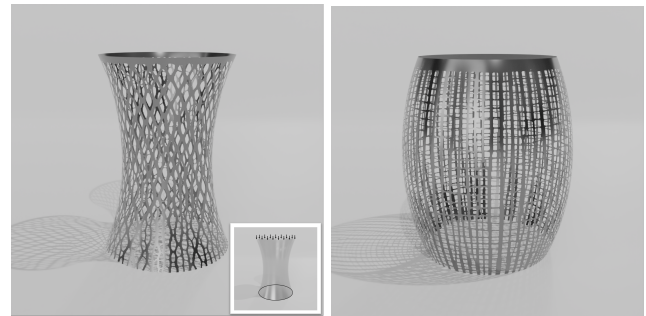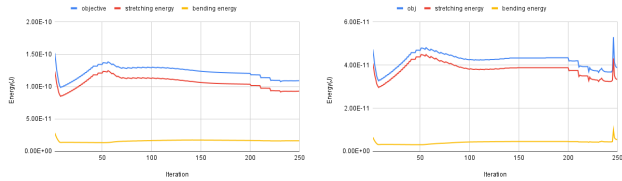
Figure 11: Left: the convergence plot of the concave hyperboloid cylinder. Right: the convergence plot of the convex hyperboloid cylinder.

Hyperboloid cylinder By fixing the bottom of the hyperboloid cylinder nodes and adding a distributed load of $0.0001N$ on the top, we optimize the density distribution on concave and convex hyperboloid cylinders which are both $3m$ tall, see Figure 10. The concave cylinder produces a network consisting of connecting rhombi while the convex cylinder produces a network consisting of rectangles. The optimizer automatically generates the solid ring on the top of the cylinders to maximize the stiffness around the force load. These two patterns match the design of durable stools in the real world. The convergence plots are given in 11.

Figure 12: Optimization intermediate states of the Stanford bunny at iteration 1, 20, 100 and 250. The boundary condition is indicated in the first picture, where the bottom nodes of the bunny are fixed and loads are applied on the head and the back.

Stanford bunny Our method also works on more complex geometries like the Stanford bunny, shown in Figure 12 with the convergence plot in Figure 13. We fixed the bottom nodes of the bunny and applied distributed loads of $0.1N$ on the head and the back of the bunny. Concentrated density formed around the head and the back area where the force loads are
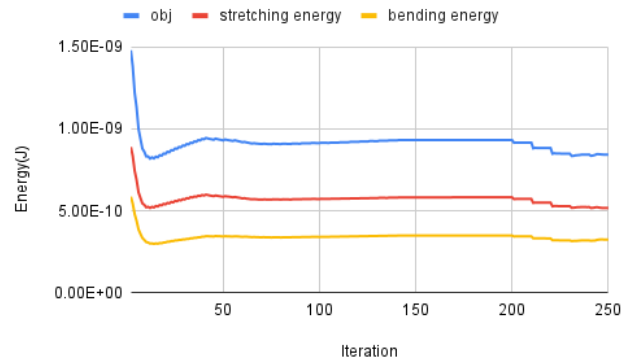

Figure 13: The convergence plot of the bunny example.

applied, while grid-like structures span around the chest and buttock area.

Odonata Wing In this example, we show that our method can produce detailed vein-like structures on an Odonata wing with out-of-plane forces. In Figure 14 with convergence plots in Figure 15, the design domain is a shell shaped like the Odonata wing with the middle nodes lifted a small amount (as illustrated by the inset of the bottom figure). The leftmost nodes on the boundary are fixed in both cases which is similar to how wings are attached on odonata. In the top figure, the distributed loads are applied on the right bottom boundary nodes along the normal direction with 5 degrees of out-of-plane component into the image plane. Long beams with high densities are formed in the middle and bottom of the plane, traversing horizontally and tapering towards the right end. In the bottom figure, distributed forces pointing into the image plane with a linear increment from left to right are applied to every node. We observe that a main beam travels horizontally in the middle and it branches out like fractals over the entire domain. Although in real life, the force load applied to the Odonata wing is constantly changing, here we provide the optimized structure under two arbitrary loads with out-of-plane force components to obtain some insights.

5. Conclusion

This paper presents a nonlinear topology optimization algorithm on thin shells to obtain complex structures. The algorithm embodied a differentiable, nonlinear thin shell solver to carry out sensitivity analysis and density evolution on a shell mesh. A density filter was designed to coerce binary structures. We validated our approach on different test scenarios of optimizing nonlinear structures, exploring the bending-stretching tradeoff, and large nonlinear deformation, as well as generating high-resolution shell structures.

Currently, our approach has several aspects of limitations. First, our current thin-shell solver cannot handle element inversion, hindering it from solving shells with a large in-plane compression. Strain-limiting methods or invertible
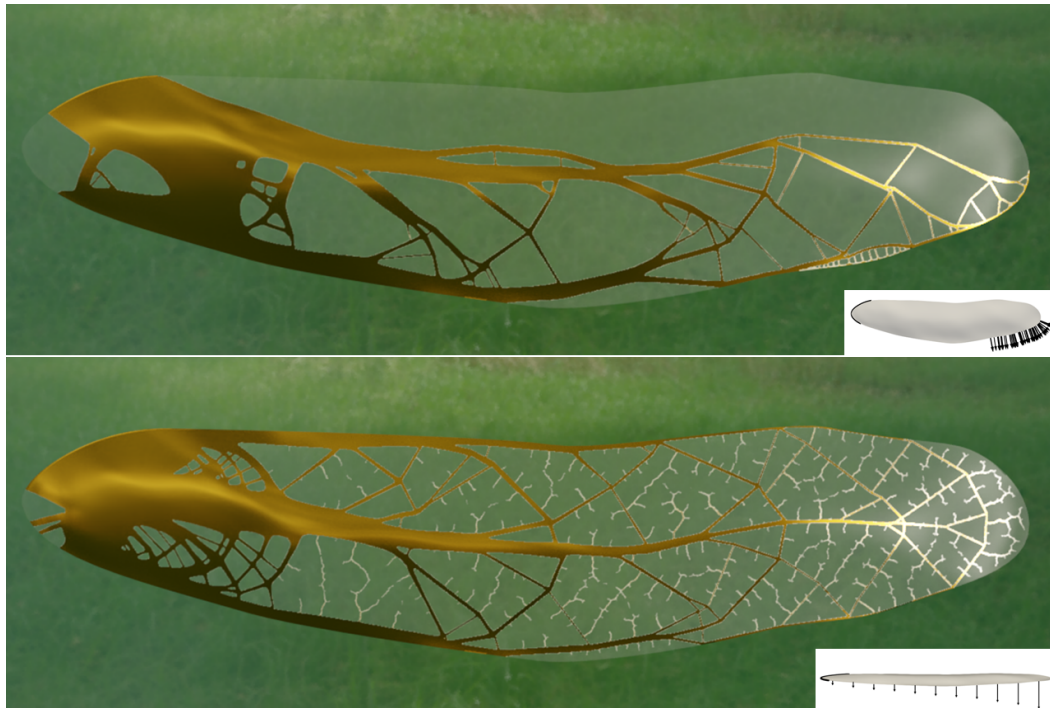
Figure 14: Odonata wing optimization results with two different loading cases.
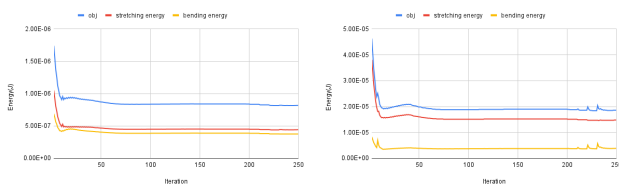

Figure 15: Left: the convergence plot of the Odonata wing example with pulling force on the bottom right boundary. Right: the convergence plot of the Odonata wing example with downward pushing forces on the entire domain.

elastic solvers (e.g., [54]) will be considered to enhance the robustness of the current method. Second, our method does not optimize shape. Due to the algorithmic complexities of updating mesh elements, it is currently challenging to co-optimize mesh geometry and topology in a unified framework. It will be interesting to further explore thin-shell solvers that can work on other shell representations such as particles and implicit surfaces to explore the possibilities of shape-density co-optimization. Third, devising high-performance multigrid shell solvers is also an immediate next step to facilitate super-resolution shell optimization. Last, our current method does not support nonmanifold geometries, which prevents the tackling of many interesting shell structures such as foams and bubble clusters. One of our future directions is to explore the nonmanifold shell solver and its topology optimization.

References

[1] E. A. Träff, O. Sigmund, N. Aage, Topology optimization of ultra high resolution shell structures, Thin-Walled Structures 160 (2021) 107349.

[2] T. Otani, W. Sumihira, Y. Kobayashi, M. Tanaka, Density-based topology optimization of thin plate structure with geometric nonlinearity using a three-dimensional corotational triangle element formulation, Structural and Multidisciplinary Optimization 65 (2022) 282.

[3] X. Jiang, W. Zhang, C. Liu, Z. Du, X. Guo, An explicit approach for simultaneous shape and topology optimization of shell structures, Applied Mathematical Modelling 113 (2023) 613–639.

[4] C. Multiphysics, Introduction to comsol multiphysics®, COMSOL Multiphysics, Burlington, MA, accessed Feb 9 (1998) 2018.

[5] F. Brezzi, K.-J. Bathe, M. Fortin, Mixed-interpolated elements for reissner–mindlin plates, International Journal for Numerical Methods in Engineering 28 (1989) 1787–1801.

[6] P.-S. Lee, K.-J. Bathe, Development of mitc isotropic triangular shell finite elements, Computers & Structures 82 (2004) 945–962.

[7] Y. Lee, P.-S. Lee, K.-J. Bathe, The mitc3+ shell element and its performance, Computers & Structures 138 (2014) 12–23.

[8] P.-S. Lee, H.-C. Noh, K.-J. Bathe, Insight into 3-node triangular shell finite elements: the effects of element isotropy and mesh patterns, Computers & Structures 85 (2007) 404–418.

[9] H.-M. Jeon, Y. Lee, P.-S. Lee, K.-J. Bathe, The MITC3+ shell element in geometric nonlinear analysis, Computers & Structures 146 (2015) 91 – 104.

[10] D. Terzopoulos, J. Platt, A. Barr, K. Fleischer, Elastically deformable models, in: Proceedings of the 14th annual conference on Computer graphics and interactive techniques, 1987, pp. 205–214.

[11] D. Baraff, A. Witkin, Large steps in cloth simulation, in: Proceedings of the 25th annual conference on Computer graphics and interactive techniques, 1998, pp. 43–54.

[12] E. Grinspun, A. N. Hirani, M. Desbrun, P. Schröder, Discrete shells, in: Proceedings of the 2003 ACM SIGGRAPH/Eurographics symposium on Computer animation, Citeseer, 2003, pp. 62–67.

[13] Y. Gingold, A. Secord, J. Y. Han, E. Grinspun, D. Zorin, A discrete model for inelastic deformation of thin shells, in: ACM SIGGRAPH/Eurographics symposium on computer animation, Citeseer, 2004.

[14] R. Bridson, S. Marino, R. Fedkiw, Simulation of clothing with folds and wrinkles, in: ACM SIGGRAPH 2005 Courses, 2005, pp. 3–es.

[15] C. Weischedel, A discrete geometric view on shear-deformable shell models, Ph.D. thesis, University of Göttingen, Wilhelmsplatz 1, 37073 Göttingen, Germany, 2012.

[16] H.-Y. Chen, A. Sastry, W. M. van Rees, E. Vouga, Physical simulation of environmentally induced thin shell deformation, ACM Transactions on Graphics (TOG) 37 (2018) 1–13.

[17] M. P. Bendsøe, Optimal shape design as a material distribution problem, Struct Multidiscipl Optim 1 (1989) 193–202.

[18] M. P. Bendsoe, O. Sigmund, Topology optimization: theory, methods, and applications, Springer Science & Business Media, 2003.

[19] O. Sigmund, K. Maute, Topology optimization approaches, Structural and Multidisciplinary Optimization 48 (2013) 1031–1055.

[20] A. Clausen, N. Aage, O. Sigmund, Topology optimization of coated structures and material interface problems, Computer Methods in Applied Mechanics and Engineering 290 (2015) 524–541.

[21] A. Clausen, E. Andreassen, O. Sigmund, Topology optimization for coated structures, in: Li Q, Steven GP, Zhang Z, editors Proceedings of the 11th World Congress on Structural and Multidisciplinary Optimization, 2015, pp. 7–12.

[22] Y. Wang, Z. Kang, A level set method for shape and topology optimization of coated structures, Computer Methods in Applied Mechanics and Engineering 329 (2018) 553–574.

[23] G.-W. Jang, S. Kambampati, H. Chung, H. A. Kim, Configuration optimization for thin structures using level set method, Structural and Multidisciplinary Optimization 59 (2019) 1881–1893.

[24] R. Dienemann, A. Schumacher, S. Fiebig, Topology optimization for finding shell structures manufactured by deep drawing, Structural and Multidisciplinary Optimization 56 (2017) 473–485.

[25] Y. Zhou, T. Nomura, E. M. Dede, K. Saitou, Topology optimization with wall thickness and piecewise developability constraints for foldable shape-changing structures, Structural and Multidisciplinary Optimization 65 (2022) 118.

[26] J. Wu, A. Clausen, O. Sigmund, Minimum compliance topology optimization of shell–infill composites for additive manufacturing, Computer Methods in Applied Mechanics and Engineering 326 (2017) 358–375.

[27] J. Wu, N. Aage, R. Westermann, O. Sigmund, Infill optimization for additive manufacturing–approaching bone-like porous structures, IEEE Transactions on Visualization and Computer Graphics 24 (2018) 1127–1140.

[28] H. Liu, Y. Hu, B. Zhu, W. Matusik, E. Sifakis, Narrow-band topology optimization on a sparsely populated grid, ACM Transactions on Graphics (TOG) 37 (2018) 1–14.

[29] F. Feng, S. Xiong, Z. Liu, Z. Xian, Y. Zhou, H. Kobayashi, A. Kawamoto, T. Nomura, B. Zhu, Cellular topology optimization on differentiable voronoi diagrams, International Journal for Numerical Methods in Engineering 124 (2023) 282–304.

[30] U. Ringertz, Numerical methods for optimization of nonlinear shell structures, Structural optimization 4 (1992) 193–198.

[31] R. Ansola, J. Canales, J. A. Tarrago, J. Rasmussen, An integrated approach for shape and topology optimization of shell structures, Computers & structures 80 (2002) 449–458.

[32] J. Stegmann, E. Lund, Nonlinear topology optimization of layered shell structures, Structural and Multidisciplinary Optimization 29 (2005) 349–360.

[33] C. F. Hvejsel, E. Lund, Material interpolation schemes for unified topology and multi-material optimization, Structural and Multidisciplinary Optimization 43 (2011) 811–825.

[34] S. N. Sørensen, E. Lund, Topology and thickness optimization of laminated composites including manufacturing constraints, Structural and Multidisciplinary Optimization 48 (2013) 249–265.

[35] T. Ho-Nguyen-Tan, H.-G. Kim, An efficient method for shape and topology optimization of shell structures, Structural and Multidisciplinary Optimization 65 (2022) 1–28.

[36] P. Kang, S.-K. Youn, Isogeometric topology optimization of shell structures using trimmed nurbs surfaces, Finite Elements in Analysis and Design 120 (2016) 18–40.

[37] Z. Gao, P. Liu, Z. Sun, K. Yang, Y. Luo, Manifold-based material field series expansion method for topology optimization on free-form surfaces, Computational Mechanics (2022) 1–19.

[38] M. Shimoda, H. Nakayama, S. Suzaki, R. Tsutsumi, A unified simultaneous shape and topology optimization method for multi-material laminated shell structures, Structural and Multidisciplinary Optimization 64 (2021) 3569–3604.

[39] T. Buhl, C. B. Pedersen, O. Sigmund, Stiffness design of geometrically nonlinear structures using topology optimization, Structural and Multidisciplinary Optimization 19 (2000) 93–104.

[40] F. Wang, B. S. Lazarov, O. Sigmund, J. S. Jensen, Interpolation scheme for fictitious domain techniques and topology optimization of finite strain elastic problems, Computer Methods in Applied Mechanics and Engineering 276 (2014) 453–472.

[41] F. Chen, Y. Wang, M. Y. Wang, Y. Zhang, Topology optimization of hyperelastic structures using a level set method, Journal of Computational Physics 351 (2017) 437–454.

[42] T. E. Bruns, D. A. Tortorelli, An element removal and reintroduction strategy for the topology optimization of structures and compliant mechanisms, International journal for numerical methods in engineering 57 (2003) 1413–1430.

[43] R. Behrou, R. Lotfi, J. V. Carstensen, F. Ferrari, J. K. Guest, Revisiting element removal for density-based structural topology optimization with reintroduction by heaviside projection, Computer Methods in Applied Mechanics and Engineering 380 (2021) 113799.

[44] P. D. Dunning, On the co-rotational method for geometrically nonlinear topology optimization, Structural and multidisciplinary optimization 62 (2020) 2357–2374.

[45] M. Skouras, B. Thomaszewski, B. Bickel, M. Gross, Computational design of rubber balloons, in: Computer Graphics Forum, volume 31, Wiley Online Library, 2012, pp. 835–844.

[46] X. Chen, X. Ni, B. Zhu, B. Wang, B. Chen, Simulation and optimization of magnetoelastic thin shells, ACM Transactions on Graphics (TOG) 41 (2022) 1–18.

[47] J. Pérez, M. A. Otaduy, B. Thomaszewski, Computational design and automated fabrication of kirchhoff-plateau surfaces, ACM Transactions on Graphics (TOG) 36 (2017) 1–12.

[48] W. Li, A. Zheng, L. You, X. Yang, J. Zhang, L. Liu, Rib-reinforced shell structure, in: Computer Graphics Forum, volume 36, Wiley Online Library, 2017, pp. 15–27.

[49] F. Gil-Ureta, N. Pietroni, D. Zorin, Reinforcement of general shell structures, ACM Transactions on Graphics (TOG) 39 (2020) 1–19.

[50] J. Panetta, M. Konaković-Luković, F. Isvoranu, E. Bouleau, M. Pauly, X-shells: A new class of deployable beam structures, ACM Transactions on Graphics (TOG) 38 (2019) 1–15.

[51] J. Panetta, F. Isvoranu, T. Chen, E. Siéfert, B. Roman, M. Pauly, Computational inverse design of surface-based inflatables, ACM Transactions on Graphics (TOG) 40 (2021) 1–14.

[52] Y. Ren, U. Kusupati, J. Panetta, F. Isvoranu, D. Pellis, T. Chen, M. Pauly, Umbrella meshes: elastic mechanisms for freeform shape deployment, ACM Transactions on Graphics 41 (2022) 1–15.

[53] R. Chandra, L. Dagum, D. Kohr, R. Menon, D. Maydan, J. McDonald, Parallel programming in OpenMP, Morgan kaufmann, 2001.

[54] J. Teran, E. Sifakis, G. Irving, R. Fedkiw, Robust quasistatic finite elements and flesh simulation, in: Proceedings of the 2005 ACM SIGGRAPH/Eurographics symposium on Computer animation, 2005, pp.

181–190.

[55] Y. Chen, T. A. Davis, W. W. Hager, S. Rajamanickam, Algorithm 887: Cholmod, supernodal sparse cholesky factorization and update/downdate, ACM Transactions on Mathematical Software (TOMS) 35 (2008) 1–14.

[56] B. Bourdin, Filters in topology optimization, International journal for numerical methods in engineering 50 (2001) 2143–2158.

[57] F. Wang, B. S. Lazarov, O. Sigmund, On projection methods, convergence and robust formulations in topology optimization, Structural and Multidisciplinary Optimization 43 (2011) 767–784.

[58] J. Dumas, Mma, `https://github.com/jdumas/mma`, 2018.

[59] K. Svanberg, The method of moving asymptotes—a new method for structural optimization, Int J Numer Methods Eng 24 (1987) 359–373.

[60] J. K. Guest, Topology optimization with multiple phase projection, Computer Methods in Applied Mechanics and Engineering 199 (2009) 123–135.

[61] Y. Li, X. Li, M. Li, Y. Zhu, B. Zhu, C. Jiang, Lagrangian–eulerian multidensity topology optimization with the material point method, International Journal for Numerical Methods in Engineering 122 (2021) 3400–3424.